EES Catalysis

Accepted Manuscript

This article can be cited before page numbers have been issued, to do this please use: A. Yoon, F. Yang, J. Poon, S. W. Chee and B. Roldan Cuenya, *EES Catal.*, 2026, DOI: 10.1039/D5EY00354G.

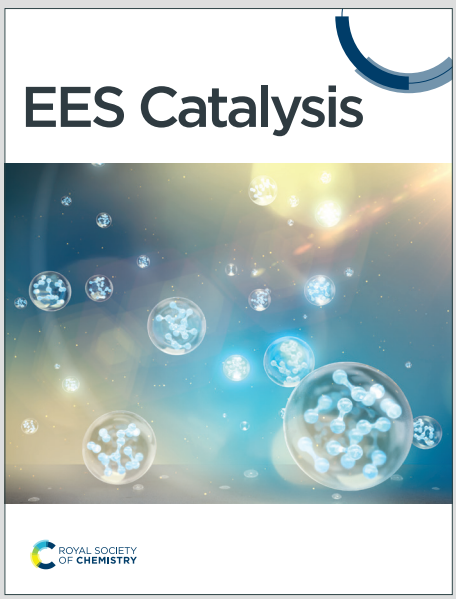

ROYAL SOCIETY OF CHEMISTRY

View Article Online
DOI: 10.1039/D5EY00354G

Broader Context Statement

Climate change concerns have spurred a growing interest in developing environmentally friendly technologies for green energy generation and storage in the form of chemical bonds. The latter includes the re-utilization of CO_2 via electrocatalytic reduction (CO_2RR) into value-added chemicals and fuels. Copper (Cu) is an important catalyst material that is key to our efforts to revalorize CO_2 back into useful hydrocarbons. Generally, oxide-derived Cu pre-catalysts are better producing hydrocarbons compared to metallic Cu pre-catalysts, but the specific structure-property relationships remain difficult to unravel due to complex morphological changes experienced by the catalysts during reaction. The present manuscript clarifies a highly controversial aspect in the field of CO_2RR, namely, whether there is a role of pre-catalyst shape on the electrocatalytic activity and more importantly, selectivity using unique approach combining electrochemical liquid cell transmission electron microscopy (TEM), identical location TEM/electron diffraction and electron tomography. Our work unveils that regardless of the specific well-defined initial shape selected, in this case, cubic versus octahedral pre-catalysts, the reaction selectivity is very similar after even relatively short reaction times (75 minutes) due to the drastic structural transformations that these materials experience in the course of the reaction.

Does the Pre-catalyst Shape Matter in the Electrocatalytic Reduction of CO_2? Tracking Mosaicity and Porosity Development in Cu_2O Particles during Reaction

View Article Online
DOI: 10.1039/D5EY00354G

Received 00th January 20xx,
Accepted 00th January 20xx

DOI: 10.1039/x0xx00000x

Aram Yoon[a, †], Fengli Yang[a], Jeffrey Poon[a, ††], See Wee Chee*[a], Beatriz Roldan Cuenya*[a]

Copper (Cu) is an important catalyst material for driving the electrocatalytic reduction of CO_2 (CO_2RR) into hydrocarbons. Particularly, oxide-derived Cu catalysts generally exhibit higher catalytic selectivity toward hydrocarbons compared to metallic Cu pre-catalysts but the degree to which the initial pre-catalyst surface facet structure affects the catalyst activity and selectivity remains unclear. This is in part due to due to the non-controlled dynamic and kinetic transformations that these catalysts undergo during electrocatalysis. In this study, we followed the restructuring of cubic and octahedral Cu_2O pre-catalyst particles during CO_2RR using liquid cell transmission electron microscopy and ex situ identical location electron diffraction. We found that both shapes fragment into smaller interconnected Cu domains with different preferred domain orientations to accommodate the strain resulting from the lattice contraction caused by the abrupt removal of oxygen during CO_2RR. Nonetheless, a comparison of the product selectivity between the electrodeposited Cu_2O cubes and octahedra with initially similar sizes and surface loadings but different shape, unveiled minimal differences in their catalytic performance. Hence, our results indicate that the structural complexity that arises during the initial stages of the CO_2RR, including particle fragmentation creating mosaicity and porosity and the concurrent re-deposition altering the working catalyst distribution are the primary processes controlling the performance of oxide-derived Cu catalysts.

Introduction

The electrocatalytic reduction of carbon dioxide (CO_2RR) into valuable chemicals such as hydrocarbons and alcohols is gaining significant attention due to its potential contribution to the revalorization of the green gas CO_2. So far, notable progress has been made in improving activity and selectivity through advanced catalyst design based on controlling the catalyst composition and morphology, and electrolyte chemistry[1–3], but the origins of such improvements are not always well-understood. The fundamental challenge with elucidating the controlling parameters lies in our insufficient insight into the metastable catalysts' morphologies that exist under reaction conditions. Significant restructuring, such as fragmentation, detachment and re-deposition takes place during CO_2RR,[2,4] accompanying the reduction of the oxide species in the pre-catalyst. This complicates the efforts to interpret the catalyst performance based on the pre-catalyst morphology, which in most cases only determines the dynamics of the transformations first towards achieving the metastable "steady-state" and any undesired subsequent kinetically-driven deactivation processes. In-depth understanding of the restructuring that takes place under electrocatalytic working conditions will allow us to better rationalize the catalytic behavior of these materials.

Cu oxide is a common starting pre-catalyst material for CO_2RR because the resulting, mostly reduced metallic Cu catalysts had been found to possess exceptional selectivity towards C_{2+} products as compared to their counterparts that were prepared directly as metallic Cu. For example, it was demonstrated that Cu catalysts generated from thermally grown-Cu_2O steered the selectivity of CO or CO_2 electrocatalytic reduction toward longer chain hydrocarbons[5–11]. Deliberately oxidizing the surface of Cu foils and Cu nanoparticles (NPs) through oxidative plasma treatment[12] or pulsed electrochemistry[13,14] also led to enhanced C_{2+} selectivity. In general, studies involving oxidized pre-catalysts revealed a high degree of defect formation, such as grain boundaries, edges and voids, which remained present during the reaction[7,15–18]. Thus, it has been hypothesized that these defective morphologies, generated from the reduction of Cu oxide to metallic Cu may be responsible for the selectivity enhancement. In particular, a rough morphology with a higher density of undercoordinated sites after reconstruction was considered to promote C-C coupling and the generation of longer-chain hydrocarbons[18–28]. The rougher morphology of oxide-derived Cu can also stabilize dissolved oxygen during the initial stages of CO_2RR and the loss of such species may explain the decreased selectivity observed upon extended (>1 h) operation in alkaline electrolytes[26]. Another aspect that may be related to the favorable catalytic performance in these materials is the co-existence of highly disordered Cu(0)/Cu(I)/Cu(II) species which can be (re-)generated during the reaction[14]. These results are leading to new discussions regarding whether the hydrocarbon selectivity reported for different Cu single crystals should be attributed to active sites on the flat planar surfaces or caused by favorable defects in the crystal structure, such as favorable steps and kink sites, created during surface reconstruction under reaction conditions. [25,26,29]

The idea that specific surfaces of bulk Cu crystals have different selectivity can be traced back to the pioneering work by Hori.[30] Nonetheless, it should be noted that an electropolishing treatment was applied to these single crystal surfaces before CO_2RR, which is known to lead to enhanced roughening and surface re-structuring. While recent findings had suggested that similar facet dependences extend to shape-controlled Cu particles,[31–33] whether these "shape effects" can be attributed to other factors, such as to distinct ligand residues available on the surface of the particles prepared using colloidal methods remains to be clarified. Here, one must consider

[a] *Department of Interface Science, Fritz Haber Institute of the Max Planck Society, Faradayweg 4-6, Berlin 14195, Germany*
** Corresponding authors: swchee@fhi-berlin.mpg.de; roldan@fhi-berlin.mpg.de*
† Currently at Institut de Physique et Chimie des Matériaux de Strasbourg (IPCMS), Strasbourg, France
†† Currently at Elsevier Ltd, Kidlington, Oxfordshire, Great Britain
Supplementary Information available: Experimental methods and supplementary figures. See DOI: 10.1039/x0xx00000x

that the initial pre-catalyst particles are prepared ex situ, and so, even if they are described as metallic, they will still have an oxide surface layer due to air exposure and the characteristics and reduction behavior of these oxidized surfaces in turn will depend on the initial particle size, facet orientation and whether any residual ligand remains from the synthesis route employed. Some degree of surface reduction will, therefore, inevitably occur during operation. Moreover, in alkaline electrolytes, these nanoparticles can form surface Cu hydroxides when exposed to the aqueous alkali electrolyte environment. The main distinction between these "metallic" particle pre-catalysts and the here described oxide-derived Cu particles is that a much rougher (and likely active) particle morphology will result for the latter since the reaction-induced reduction not only alters the particle surface but also its bulk during CO_2RR. The lack of sufficient experimental data on well-defined pre-catalyst materials, the extensive restructuring experienced by oxidized Cu pre-catalysts, and the technical difficulties with probing these highly corrugated structures, however, hinder our ability to make a solid bridge to theoretical modeling and the resulting mechanistic understanding of the working structures in oxide-derived catalysts.

A promising way to track the catalyst's evolution under reaction conditions is liquid cell transmission electron microscopy (TEM)[34–40]. Particularly, our group used the method to visualize Cu_2O cubes with {100} surface termination undergoing fragmentation and transforming into nanoporous cubic particles made up of Cu nanograins and secondary re-deposited particles during CO_2RR[36]. Our results revealed how intricate interplays between the initial pre-catalyst loading, and the subsequent re-structuring led to different hydrocarbon selectivities. We also noticed that the resultant fragmented morphologies mimicked the structural changes reported by others for other oxide-derived catalysts.[6,17,28]

In the present study, we thoroughly characterized the re-structuring and morphological features found on cubic pre-catalysts with initial {100} facets and on octahedral Cu_2O particles with {111} surface termination with *in situ* and *ex situ* TEM measurements to reveal different aspects of the catalyst transformation to establish correlations with their CO_2RR selectivity. These pre-catalysts were synthesized using electrodeposition to have well-defined surfaces without the use of strong binding ligands, and with controlled loading to avoid the ambiguity in particle dispersion that comes with drop-casted samples. Particularly, we focus on the structural changes that occur within the first hour of reaction where the most drastic restructuring occurs.[36] We show that despite the restructured particles showing preferred domain orientations dictated by the initial pre-catalyst shape, the selectivity values obtained for the cubic and octahedral particles are were similar, indicating that the initial shape of the pre-catalyst is not the most decisive parameter determining the subsequent reactivity behavior.

Results and Discussion

Figures 1a and b describe the morphologies of the size-controlled Cu_2O cubes and octahedra obtained after electrodeposition. The TEM images and electron diffraction data confirmed that the cubes and octahedra are single crystals. Figure 1c shows a cubic particle oriented along [100], and Figure 1e an octahedron particle oriented along [110].

The electron diffraction patterns in Figures 1d and f are consistent with Cu_2O. The surface normal of the cube is {100}, and that of the octahedron is {111}. Octahedra expose a small portion of {001} facets by the truncation of their top and bottom facets (Figure 1e). Some threading dislocations along the growth direction can also be observed in the octahedra. To gain insight into possible effects of the as-synthesized shape during CO_2RR, while minimizing the contribution of other structural/morphological factors, we meticulously tuned the synthesis parameters to generate pre-catalyst samples with similar initial size, loading and support. The success of this approach was corroborated by our SEM data, unveiling shaped nanoparticles of uniform size and shape that are homogeneously deposited across the carbon support, as seen in the histograms in Figure 1g. Figure 2 describes how catalyst morphology changes due to reaction as observed using ex situ and in situ EM. As indicated by the SEM images Figure 2(a, b) and Figure 2(d, e) comparing the samples before and after reaction, the defined shapes of the pre-catalysts are no longer distinguishable after the electrochemical reaction of CO_2RR. Figure 2c and f show images obtained from electrochemical cell TEM (EC-TEM) experiments capturing the evolution of the pre-catalysts during CO_2RR. The image sequences were recorded continuously under the flow of CO_2-saturated 0.1M $KHCO_3$ and at the constant potential of -1.0 V_{RHE}. Both types of Cu_2O particles restructured at a very early stage of CO_2RR (within the duration of the initial linear sweep voltammetry, which was about 1 min long). Figure 2c shows the restructuring of the Cu_2O cubes, which followed the processes of fragmentation and re-deposition/agglomeration as we had previously reported for similarly prepared samples of different initial size distributions.[36] Analogous fragmentation and the re-deposition/agglomeration of small nanoparticles were also observed for the octahedral-shaped Cu_2O particles with applied potential. (Figures 2f).

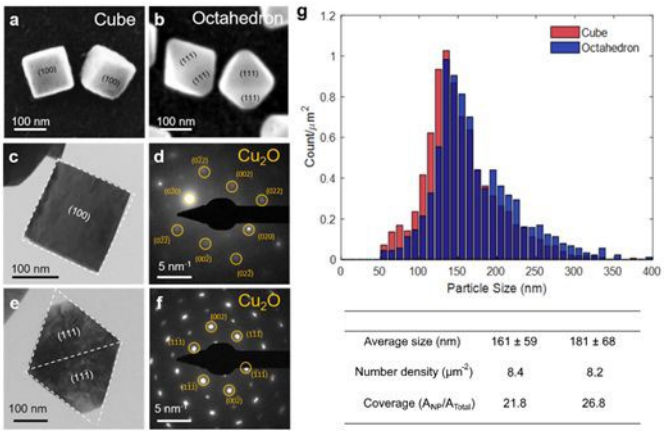

	Cube	Octahedron
Average size (nm)	161 ± 59	181 ± 68
Number density (μm^{-2})	8.4	8.2
Coverage (A_{NP}/A_{total})	21.8	26.8

Figure 1 As-prepared Cu_2O cubes and truncated octahedra: SEM images of (a) cubes and (b) octahedra nanoparticle pre-catalysts deposited on glassy carbon. The cubes and the octahedra were also deposited on the liquid cell TEM chips. TEM images of (c) a cube and (e) an octahedron and their corresponding electron diffraction patterns in (d), (f), respectively. (g) Histograms and table comparing the size and particle density of the cube and octahedra pre-catalyst particles.

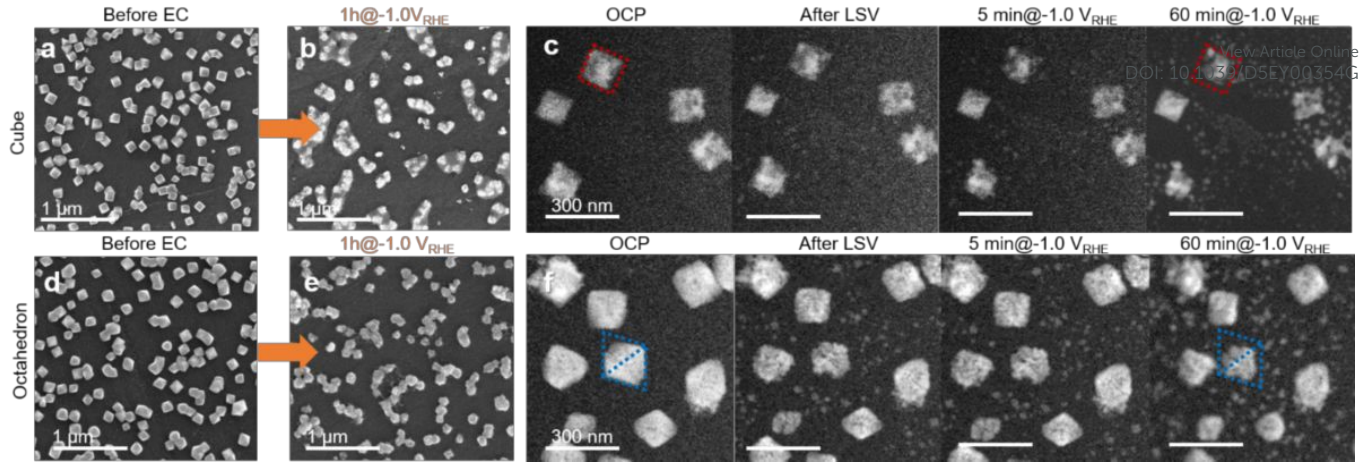

Figure 2 Ex situ SEM and in situ EC-TEM images showing restructuring of cubic and octahedral Cu_2O under CO_2 electrocatalytic-reduction conditions. SEM images of the Cu_2O cubes on GC support before (a) and after (b) CO2RR for 1 hour at -1.0 V_{RHE} in CO_2-saturated 0.1M $KHCO_3$. (c) In situ EC-TEM images of cubes deposited on EC-TEM chip showing the restructuring process at open circuit potential (OCP), after linear sweep voltammetry from OCP to -1.0 V_{RHE} (15 mV/s), and after 5 min and 1-hour CO_2RR while holding the potential constant at -1.0 V_{RHE}. The same set of Cu_2O octahedra is presented in (d-e). (f) In situ EC-TEM images of octahedra recorded during reaction. The recorded videos for (c) and (f) are provided as Supplementary Movie S1 and S2 respectively.

Next, to examine the re-structured particles in detail, the liquid cell was disassembled after the *in situ* experiment and the samples were quickly transferred back into the TEM to minimize air exposure. Figure 3 shows *ex situ* high resolution TEM images of the same cube and octahedron before and after electrolysis. The images show that the reduction resulted in the breakup of the original single-crystalline Cu_2O pre-catalysts into smaller interconnected domains of Cu and lead to the fragmented particles having rough topology (Figures 3a, b and 3c, d). In addition, the restructured catalysts retained preferred orientation from the cubic and octahedral pre-catalysts. The 10 % reduction in particle size can be explained by the reduction of Cu_2O to metallic Cu under applied cathodic potentials and is consistent with the difference in the lattice parameters of the two phases (a_{Cu2O} = 4.27 Å, a_{Cu} = 3.61 Å). Figures 3e and f show high-resolution TEM images taken at the surface of the cubic particles before and after CO_2RR. These high-resolution images further show that some of the domains retain {100} and {111} orientation toward the surface direction after restructuring but did not retain the original surface termination. The flat Cu_2O(100) surface turned into a rugged surface consisting of smaller Cu domains that have their Cu (100) planes oriented generally towards the surface normal direction after fragmentation (Figure 3f). Cu_2O octahedral particles with flat (111) surface termination (Figure 3g) formed rough surfaces with domains with their Cu(111) surface oriented to the surface normal as shown in Figure 3h.

To confirm that such preferred domain orientations extend over the entire particle, we measured the electron diffraction pattern of the whole particle and visualized the texture of the restructured domains. Radial intensity distribution of the diffraction patterns in Figures 3(m, n) show peaks that match the known lattice parameters of Cu_2O and Cu (bars in Figure 3m and n). Here, the dominant metallic Cu intensities in the electron diffraction patterns also confirm that we were largely able avoid significant artifacts from our quick sample transfer in air back to the TEM after the CO_2RR experiment. Next, we evaluated the overall mosaicity of the fragmented catalyst particles using their electron diffraction patterns as shown in Figures 3i-l. The angular distribution of the Cu_2O{200} and Cu{200} diffraction

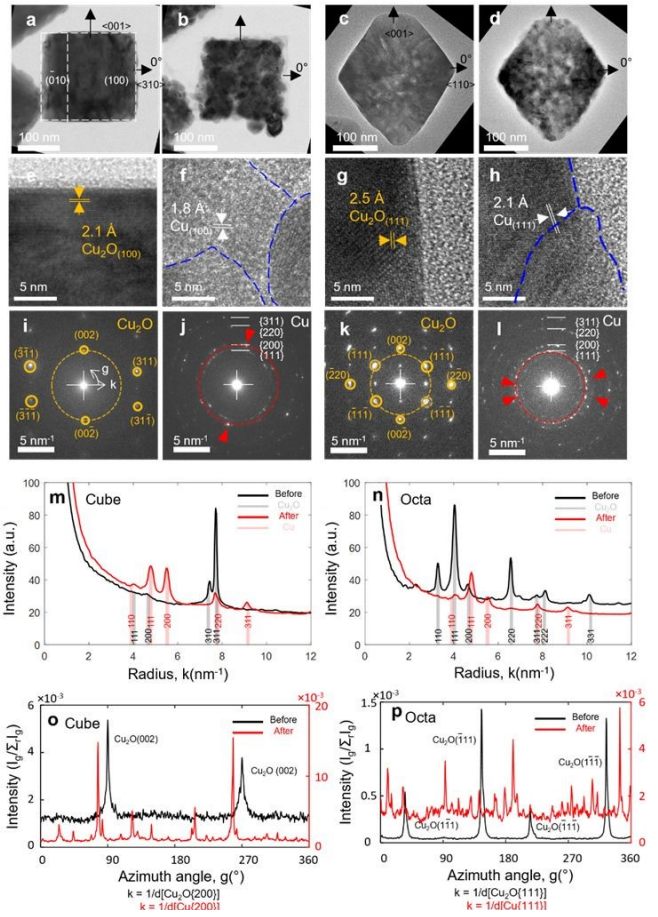

Figure 3 Texture and topography of the cubes and octahedra before and after CO_2RR. TEM images of a cube (a,b) and an octahedron (c,d) before (a,c) and after (b,d) CO_2RR show volume contraction and fragmentation after reaction. High-resolution images show the surface termination of (e) a cubic particle, (f) a fragmented cubic particle, (g) an octahedral particle, and (h) a fragmented octahedral particle. Diffraction patterns show single crystal patterns of Cu_2O in (i) and (k), and polycrystalline ring patterns of Cu in (j) and (l). (m) and (n) are the radial intensity of the Cu_2O (before CO_2RR) and Cu (after CO_2RR) of the cube and octahedron respectively. Angular intensity of Cu_2O{200} and Cu{200} from yellow and red circles in the diffraction patterns (i) and (j), respectively, are plotted in (o). Angular intensity of Cu_2O{111} and Cu{111} from yellow and red circles in the diffraction patterns (k) and (l), respectively, are plotted in (p).

intensity of a cube before and after reaction, marked in yellow in Figures 3i and red in Figure 3j, are plotted in Figure 3o. A cubic particle oriented with [1$\bar{3}$0] projection has {002} peaks at 90 ° and 270 ° (black line in Figure 3o) when the azimuth angle 0° is set [310] as marked in Figure 3a. The Cu{200} peaks from the fragmented cubes are also located near 90° and 270°, which aligns with Cu_2O{200} before fragmentation. Other than that, an angle of 45° was found between Cu_2O{200} and Cu{200}, whereas Cu_2O {111} was parallel to Cu{111} (Supplementary Figure S1).

The orientation preferences of the octahedra are shown by the angular distribution of Cu_2O{111} and Cu{111} diffraction intensities, marked in yellow in Fig. 3k and red in Fig. 3l, and plotted in Fig. 3p. The initial Cu_2O particle oriented with [1$\bar{1}$0] projection has {111} peaks at 35°, 145°, 215°, and 325° (black line in Figure 3p), while the Cu particle after fragmentation has peaks at 10°, 93°, 191°, 344°, and 360° (red line in Figure 3p). Cu_2O{111} peaks before CO_2RR and Cu{111} peaks after CO_2RR misaligned by roughly -20° or + 45°. These relationships can be found in several other octahedral particles we investigated, where some of them show also other relationships such as Cu_2O{111}//Cu{111} (Supplementary Figure S2). Therefore, fragmentation generates domains that retain preferred orientations commensurate with their initial surface terminations. We can further rationalize this fragmentation with preferably oriented domains in terms of the minimization of atomic displacement and strain during the abrupt loss of oxygen and lattice contraction.

In Supplementary Figure S3, we constructed an interface model based on the atomic arrangement and lattice spacings of Cu_2O and Cu described in Figure 3 to visualize the interfaces between different Cu_2O and Cu planes. The lattice spacings of Cu_2O{200} and Cu{200} are 2.14 and 1.81 Å, and those of Cu_2O{111} and Cu{111} are 2.48 and 2.09 Å. Cu_2O{100} and Cu{100} have also the same Cu-Cu ordering but with different Cu-Cu separation due to the presence of oxygen between the Cu atoms in Cu_2O. The same applies to Cu_2O{111} and Cu{111} planes. Here, certain rotation relationships between the Cu_2O and Cu lattice planes are interesting to note: the Cu_2O{001} surface is commensurate with the Cu{110} surface with 20% lattice mismatch when Cu{001} rotates 45° along [010] (Supplementary Figure S3c), which explains the rotation of the diffraction spots we see in Figures 3j and 3o. Cu_2O{111} is commensurate with Cu{110} with 3 % lattice mismatch when Cu{111} rotates 36° along [1$\bar{1}$0] (Supplementary Figure S3d), which is the case for Figure 3l and 3p. Other possible but less frequently observed orientation relations are Cu_2O{001}//Cu{111} and Cu_2O{111}//Cu{100}, as shown in Supplementary Figures S3e and f. Hence, the particles fragment to accommodate the defects created during oxide reduction and maintain intergranular connectivity by grain rotation.

Figure 4 reveals the morphological impact on the CO_2RR performance of the shaped particles. We compared the CO_2RR product selectivity of cubes and octahedra electrodeposited on GC plates for measurements performed from -0.8 to -1.2 V_{RHE} in CO_2-saturated 0.1M $KHCO_3$ after 75 minutes reaction. Faradaic efficiency (FE) in Figure 4(a, b), geometrically normalized current density (Figure 4c) and the partial current densities of the measured gas

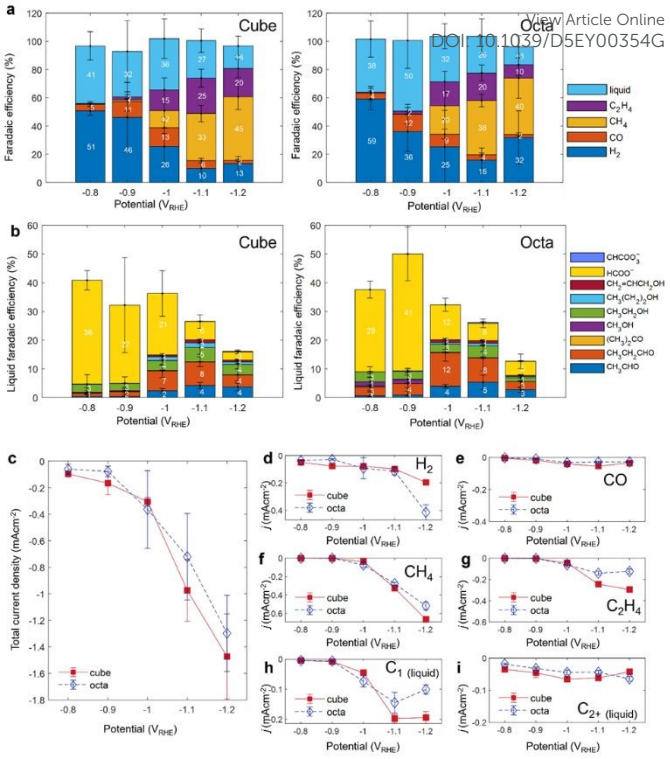

Figure 4 Comparison of the FEs and geometric current densities of Cu_2O cubes and octahedra. (a) FEs of the CO_2RR over cube (left) and octahedra (right) NPs. Liquid products are shown in (b) which are mostly formate ($HCOO^-$), ethanol (CH_3CH_2OH), propionaldehyde (CH_3CH_2CHO), and acetaldehyde (CH_3CHO). The products are measured for 75 minutes at the designated potentials from -0.8 to -1.2 V_{RHE} in CO_2-saturated 0.1 M $KHCO_3$. Each measurement was performed with a new sample and repeated 3 times to get the error bars. The total and partial current densities are plotted in (c) and (d-i) respectively.

products are plotted in Figure 4(d - i). Here, since the initial size distribution and support loading of the electrodeposited particles were kept similar, we can isolate the contribution of their geometric structure or the time-dependent evolving morphology. In general, only small differences were seen between the two differently-shaped pre-catalyst particles in the electrochemical and reaction product measurements during (for gas products) and after 75 min reaction for liquid products (results from individual injection from the online gas chromatography measurements are shown in Supplementary Figure S4) when the initially clearly distinct pre-catalyst structures have already experienced strong modifications. The largest difference is that the octahedra have a comparatively high H_2 FE (32%) at -1.2 V_{RHE}, while the cubes only produce 13 % H_2 at -1.2 V_{RHE}. C_2H_4 production has maximum yields of 25 and 20 % at -1.1 V_{RHE}, for cubes and octahedra respectively, where the former is close to what we have previously reported for similarly prepared cubes[36]. Hence, the drastic differences in the selectivity reported in previous work[31] for largely metallic Cu cubes and octahedra synthesized using encapsulating ligands, did not appear to transfer to the ligand-free but textured particles generated from shaped-Cu_2O pre-catalysts.

As shown in Figure 4d-i, there were also only minor differences in the total current density, J_{geo} and the partial current densities of the major gaseous products between the two samples. In general, the

cubes produced slightly more C_{2+} products than the octahedra. Therefore, our results indicate that despite the different facet exposures of the pre-catalysts, there is no strong surface facet dependency in oxide-derived Cu catalysts.

To identify other structural parameters that may contribute to the product selectivity, we transferred the samples from the glassy carbon working electrode onto TEM grids and performed electron tomography (Figure 5a-d) after CO_2RR (0.1 M $KHCO_3$, -1.0 V_{RHE} for 75 min). From the 3D reconstruction (Figure 5e-h), we not only see that the samples indeed show similar restructuring in both, TEM cell and conventional H-type cells, but also obtain additional descriptors such as surface area to volume ratio and porosity by slicing the volume image into the projected axis, as illustrated in Figure 5i. The projected images were then converted to binary images based on intensity and segmented to identify the pore volume within the particle. Figures 5j-m are the examples of the projected binary images from each particle, clearly showing the existence and size of the pore structure within the projected area. The quantification method is described in the supplementary information (Supplementary Figure 5).

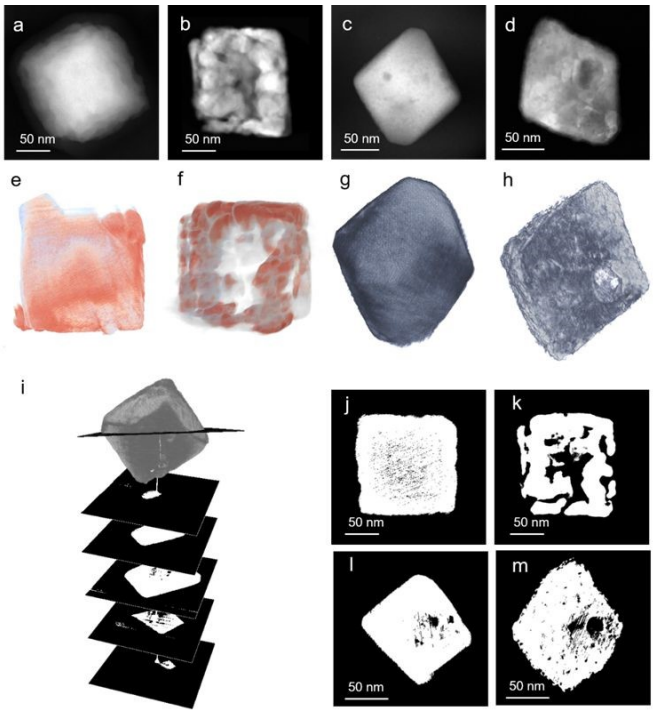

Figure 5. TEM tomography and porosity: Electron tomography image set of Cu_2O cubes (a,b) and octahedron (c,d) before (a,c) and after (b,d) CO_2RR. (e-h) The respective reconstructed volume image from the datasets in (a-d).(i) Schematic representation of the sliced images of the 3D volume to get the projected images. (j-m) Examples of the binary images of the sliced set used to calculate the material's porosity for a cube (j,k) and octahedron (l, m) before (j,l) and after (k,m) CO_2RR.

Table 1 summarizes the porosity changes of cubes and octahedra before and after the CO_2RR reaction on the carbon paper. For the cubes, the pore volume increased by 15%, from 14% to 29%, and for the octahedra, it increased by 14%, from 9% to 25%. Note that tomography was not performed on the identical particles and so, the variation in particle size, surface, and volume might be due to the choice of the particles. Even with this experimental constraint, it is clear there is a significant increase in surface area due to surface

Table 1. Surface area, volume, surface to volume ratio, and porosity of cube and octahedron before and after CO_2RR reaction

View Article Online
DOI: 10.1039/D5EY00354G

	Surface area (nm^2)	Volume (nm^3)	Surface to volume ratio	Porosity
Cube before	5.8×10^4	1.1×10^6	0.05	0.14
Cube after	2.2×10^5	2.1×10^6	0.10	0.29
Octahedron before	3.7×10^4	5.8×10^5	0.06	0.09
Octahedron after	1.0×10^4	9.7×10^5	0.11	0.25

fragmentation and the creation of the internal pores. These internal pores can further result in micro- environments with for example, locally enriched ion concentrations[43], that are different from the bulk electrolyte and might distinctively influence the catalyst activity and selectivity. Furthermore, the high density of grain boundaries and defects available within these restructured particles, which were formed during CO_2RR can serve as critical active sites for the reaction[38]. Consequently, future systematic studies focusing on the controlled engineering of porosity and defect density, combined with advanced modeling of their specific microenvironments, will be essential for refining the design principles of oxide-derived catalysts

In short, these results emphasize the material complexity that might be present and develop during electrocatalytic reactions and the dominant role that might be played by roughened internal and external surfaces, as well as intergranular defects created during the reduction of Cu_2O nanocatalysts during CO_2RR and how they control the selectivity. The abrupt and drastic structural changes seen in our well-defined (size- and shape-controlled) pre-catalysts under reaction conditions emphasize the need for thorough catalyst characterization before, during and after reaction, and caution against simplistic interpretations of catalytic performance simply based on the pre-catalyst morphology. It is also essential that we view these materials through the lens of their re-structuring behavior and how their transformation towards the active state leads to the generation of highly defective structures and secondary re-deposited particles. Moreover, the major increase in the accessible surface area for reaction that one can gain through the formation of porous structures such as the ones presented here should be considered. In cases such as the present one, not only the external outer nanoparticle surface but also inner surfaces might be accessible to the reactants, and thus, "bulk-reactivity" might set in via the porosity development.

Even though it was known that catalysts undergo restructuring, we argue that there has been insufficient characterization of the features that they encompass. For one, our microscopic studies indicate that widespread Cu re-deposition takes place on the entire carbon-based working electrode surface and so, we cannot solely focus on the pre-catalyst. Here, while small Cu NPs are mostly expected to be selective towards H_2 and CO[44], the local microenvironments they create as well as their relative density on the support can influence the probability of C-C coupling[45] and so, changes in their distribution can alter product selectivity. In this respect, we argue that the role these irregularly shaped particles, which are also often neglected in routine post-reaction analysis, play in hydrocarbon production needs to be better understood. Particularly, our earlier study showed that the biggest difference

between short- and long-duration reacted samples was the loss of particles from the working electrode surface.

Hence, while some theoretical studies are already attempting to explain how the reconstructed Cu surfaces can kinetically stabilize chemical species, such as Cu(I) species, and result in better opportunities for C-C coupling leading to enhanced C_{2+} selectivity,[22,24] further efforts taking into consideration the effects of local confinement[46,47] due to the nanoporous structure formed and the secondary NP re-deposition in between the larger porous particles are still needed to rationalize the reactivity trends obtained for oxide-derived catalysts. These results also imply that a simplistic "rational design" of the pre-catalyst structure won't lead to a desired sustained electrocatalytic performance. Instead, we need to direct the design of the metastable dynamic active working electrocatalyst and work towards extending the lifetime of such catalyst phases that are formed as a response to dynamic and kinetic processes that take place in the reaction environment. This calls for more detailed characterization of the restructured morphology obtained under different conditions and its implications on catalytic before we can rationally design catalysts for CO_2RR. Furthermore, methods that can differentiate the fraction of the activity and specific product yield arising from either the restructured pre-catalysts or the coexisting secondary NPs (formed via dissolution and redeposition) are yet to be developed. It would also be interesting to be able to achieve sufficient spatial resolution for the quantification of the microenvironment (pH/CO_2 concentration) in the pores formed in the course of the CO_2RR.

Conclusions

Here, we studied shape-, size- and loading-controlled cubic and octahedral Cu_2O pre-catalysts under CO_2RR reaction conditions to answer the question whether the initial surface facet exposure matters for oxide-derived catalysts. Our microscopic observations reveal that both, Cu_2O cubes and octahedra undergo significant fragmentation and a transformation into highly defective particles that retain their overall initial shape, but with a high degree of mosaicity and increased porosity, together with the formation of secondary NPs. Our EC-TEM observations show that an abrupt fragmentation occurs at the early stages of the CO_2RR, forming porous particles with interconnected domains of Cu, while retaining roughly the initial shape-frames of the pre-catalysts. Further crystallographic comparison of the same catalyst particles before and after CO_2RR indicates that the Cu domains partially retain the initial orientational relationships of the pre-catalysts. Preferred orientations with $Cu_2O\{100\}//Cu\{100\}$ and $Cu_2O\{111\}//Cu\{111\}$ were observed before and after CO_2RR, with Cu domains being frequently rotated by 20° or 45° with respect to the initial Cu_2O orientations.

Interestingly, and despite a clearly distinct initial particle shape, similar product selectivity trends were obtained after 75 min of CO_2 electrocatalytic reduction. This is attributed to the drastic structural transformations that underwent both types of pre-catalysts during operation, leading to the formation of highly defective porous structures with a likely large accessibility for the reactants and the generation of new catalysts due to re-deposition. The creation of grain boundaries, surface defects, and surface roughness can also influence the mobility and binding of surface absorbed molecules, which in turn impacts the stabilization of reaction intermediates during CO_2RR. Thus, our study unveils that the textural relationships in these types of catalysts impart a minimal benefit to the catalyst performance, which is rather dominated by the structural defects, secondary particles and enhanced porosity that formed during Cu_2O reduction in the course of the electrocatalytic reduction of CO_2. We expect the key to catalytic performance to be held in these diverse structures that are formed during reaction.

Author contributions

S.W.C. and B.R.C. designed and directed the experiments. A.Y performed all the TEM and electrochemistry measurements with assistance from F.L.Y and J.P.. A.Y. analyzed the data. A.Y, S.W.C and B.R.C wrote the manuscript with contributions from all authors.

Conflicts of interest

There are no conflicts to declare.

Data availability

The data supporting the findings of this study can be found within the paper and the Supplementary Information file. Raw data files are available from the corresponding authors upon reasonable request

Acknowledgements

Financial support was provided by the Bundesministerium für Bildung und Forschung (BMBF) under Grant No. 03EW0015B-CATLAB. AY thanks the Alexander von Humboldt Foundation for the postdoctoral fellowship funding and SPP 2080 "DynaKat" Early Career Research Scholarship. FY thanks the China Scholarship Council for the fellowship received and JP the Croucher Foundation, Hong Kong for their funding.

We also gratefully acknowledge Dr. Maxime Boniface and Dr. Thomas Lunkenbein of the Fritz Haber Institute of the Max Planck Society for their help regarding analysis of the electron diffraction patterns.

References

1 M. M. Sartin, Z. Yu, W. Chen, F. He, Z. Sun, Y. X. Chen and W. Huang, Effect of Particle Shape and Electrolyte Cation on CO Adsorption to Copper Oxide Nanoparticle Electrocatalysts, *J. Phys. Chem. C*, 2018, **122**, 26489–26498.

2 R. M. Arán-Ais, D. Gao, B. Roldan Cuenya, R. M. Arán-Ais, D. Gao and B. Roldan Cuenya, Structure- and Electrolyte-Sensitivity in CO2 Electroreduction, *Acc. Chem. Res.*, 2018, **51**, 2906–2917.

3 S. Nitopi, E. Bertheussen, S. B. Scott, X. Liu, A. K. Engstfeld, S. Horch, B. Seger, I. E. L. Stephens, K. Chan, C. Hahn, J. K. Nørskov, T. F. Jaramillo and I. Chorkendorff, Progress and Perspectives of Electrochemical CO2 Reduction on Copper in Aqueous Electrolyte, *Chem. Rev.*, 2019, **119**, 7610–7672.

4 S. Popović, M. Smiljanić, P. Jovanovič, J. Vavra, R. Buonsanti and N. Hodnik, Stability and Degradation Mechanisms of Copper-Based Catalysts for Electrochemical CO2 Reduction, *Angew. Chemie - Int. Ed.*, 2020, **59**, 14736–14746.

5 C. W. Li and M. W. Kanan, CO2 reduction at low overpotential on Cu electrodes resulting from the reduction of thick Cu2O films, *J. Am. Chem. Soc.*, 2012, **134**, 7231–7234.

6 C. W. Li, J. Ciston and M. W. Kanan, Electroreduction of carbon monoxide to liquid fuel on oxide-derived nanocrystalline copper, *Nature*, 2014, **508**, 504–507.

7 A. Verdaguer-Casadevall, C. W. Li, T. P. Johansson, S. B. Scott, J. T. McKeown, M. Kumar, I. E. L. Stephens, M. W. Kanan and I. Chorkendorff, Probing the Active Surface Sites for CO Reduction on Oxide-Derived Copper Electrocatalysts, *J. Am. Chem. Soc.*, 2015, **137**, 9808–9811.

8 A. Dutta, M. Rahaman, N. C. Luedi, M. Mohos and P. Broekmann, Morphology Matters: Tuning the Product Distribution of CO2 Electroreduction on Oxide-Derived Cu Foam Catalysts, *ACS Catal.*, 2016, **6**, 3804–3814.

9 D. Ren, Y. Deng, A. D. Handoko, C. S. Chen, S. Malkhandi and B. S. Yeo, Selective Electrochemical Reduction of Carbon Dioxide to Ethylene and Ethanol on Copper(I) oxide catalysts, *ACS Catal.*, 2015, **5**, 2814–2821.

10 H. Li, T. Liu, P. Wei, L. Lin, D. Gao, G. Wang and X. Bao, High-Rate CO2 Electroreduction to C2+ Products over a Copper-Copper Iodide Catalyst, *Angew. Chemie*, 2021, **133**, 14450–14454.

11 Y. Lum and J. W. Ager, Evidence for product-specific active sites on oxide-derived Cu catalysts for electrochemical CO2 reduction, *Nat. Catal.*, 2019, **2**, 86–93.

12 H. Mistry, A. S. Varela, C. S. Bonifacio, I. Zegkinoglou, I. Sinev, Y. W. Choi, K. Kisslinger, E. A. Stach, J. C. Yang, P. Strasser and B. R. Cuenya, Highly selective plasma-activated copper catalysts for carbon dioxide reduction to ethylene, *Nat. Commun.*, 2016, **7**, 12123.

13 R. M. Arán-Ais, F. Scholten, S. Kunze, R. Rizo and B. Roldan Cuenya, The role of in situ generated morphological motifs and Cu(i) species in C2+ product selectivity during CO2 pulsed electroreduction, *Nat. Energy*, 2020, **5**, 317–325.

14 J. Timoshenko, A. Bergmann, C. Rettenmaier, A. Herzog, R. M. Arán-Ais, H. S. Jeon, F. T. Haase, U. Hejral, P. Grosse, S. Kühl, E. M. Davis, J. Tian, O. Magnussen and B. Roldan Cuenya, Steering the structure and selectivity of CO2 electroreduction catalysts by potential pulses, *Nat. Catal.*, 2022, **5**, 259–267.

15 R. G. Mariano, K. McKelvey, H. S. White and M. W. Kanan, Selective increase in CO2 electroreduction activity at grain-boundary surface terminations, *Science (80-.).*, 2017, **358**, 1187–1192.

16 Y. Lum and J. W. Ager, Stability of Residual Oxides in Oxide-Derived Copper Catalysts for Electrochemical CO2 Reduction Investigated with 18O Labeling, *Angew. Chemie Int. Ed.*, 2018, **57**, 551–554.

17 C. Chen, X. Yan, Y. Wu, S. Liu, X. Sun, Q. Zhu, R. Feng, T. Wu, Q. Qian, H. Liu, L. Zheng, J. Zhang and B. Han, Thein situstudy of surface species and structures of oxide-derived copper catalysts for electrochemical CO2reduction, *Chem. Sci.*, 2021, **12**, 5938–5943.

18 L. Mandal, K. R. Yang, M. R. Motapothula, D. Ren, P. Lobaccaro, A. Patra, M. Sherburne, V. S. Batista, B. S. Yeo, J. W. Ager, J. Martin and T. Venkatesan, Investigating the Role of Copper Oxide in Electrochemical CO2 Reduction in Real Time, *ACS Appl. Mater. Interfaces*, 2018, **10**, 8574–8584.

19 J. J. Velasco-Vélez, C. H. Chuang, D. Gao, Q. Zhu, D. Ivanov, H. S. Jeon, R. Arrigo, R. V. Mom, E. Stotz, H. L. Wu, T. E. Jones, B. Roldan Cuenya, A. Knop-Gericke and R. Schlögl, On the Activity/Selectivity and Phase Stability of Thermally Grown Copper Oxides during the Electrocatalytic Reduction of CO2, *ACS Catal.*, 2020, **10**, 11510–11518.

20 R. Kas, R. Kortlever, A. Milbrat, M. T. M. Koper, G. Mul and J. Baltrusaitis, Electrochemical CO2 reduction on Cu2O-derived copper nanoparticles: Controlling the catalytic selectivity of hydrocarbons, *Phys. Chem. Chem. Phys.*, 2014, **16**, 12194–12201.

21 J.-J. J. Velasco-Velez, J.-J. J. Velasco-Velez, R. V. Mom, L.-E. E. Sandoval-Diaz, L. J. Falling, C.-H. H. Chuang, D. Gao, D. Gao, T. E. Jones, Q. Zhu, Q. Zhu, R. Arrigo, B. Roldan Cuenya, A. Knop-Gericke, A. Knop-Gericke, T. Lunkenbein, R. Schlögl and R. Schlögl, Revealing the Active Phase of Copper during the Electroreduction of CO2 in Aqueous Electrolyte by Correlating In Situ X-ray Spectroscopy and In Situ Electron Microscopy, *ACS Energy Lett.*, 2020, **5**, 2106–2111.

22 F. Dattila, R. Garclá-Muelas and N. López, Active and Selective Ensembles in Oxide-Derived Copper Catalysts for CO2Reduction, *ACS Energy Lett.*, 2020, **5**, 3176–3184.

23 J. E. Pander, D. Ren, Y. Huang, N. W. X. Loo, S. H. L. Hong and B. S. Yeo, Understanding the Heterogeneous Electrocatalytic Reduction of Carbon Dioxide on Oxide-Derived Catalysts, *ChemElectroChem*, 2018, **5**, 219–237.

24 D. Cheng, Z. J. Zhao, G. Zhang, P. Yang, L. Li, H. Gao, S. Liu, X. Chang, S. Chen, T. Wang, G. A. Ozin, Z. Liu and J. Gong, The nature of active sites for carbon dioxide electroreduction over oxide-derived copper catalysts, *Nat. Commun.*, 2021, **12**, 1–8.

25 F. Scholten, K. L. C. Nguyen, J. P. Bruce, M. Heyde and B. Roldan Cuenya, Identifying Structure–Selectivity Correlations in the Electrochemical Reduction of CO2: A Comparison of Well-Ordered Atomically Clean and Chemically Etched Copper Single-Crystal Surfaces, *Angew. Chemie Int. Ed.*, 2021, **60**, 19169–19175.

26 K. L. C. Nguyen, J. P. Bruce, A. Yoon, J. J. Navarro, F. Scholten, F. Landwehr, C. Rettenmaier, M. Heyde and B. R. Cuenya, The Influence of Mesoscopic Surface Structure on the Electrocatalytic Selectivity of CO2 Reduction with UHV-Prepared Cu(111) Single Crystals, *ACS Energy Lett.*, 2024, **9**, 644–652.

27 R. Amirbeigiarab, J. Tian, A. Herzog, C. Qiu, A. Bergmann, B.

Roldan Cuenya and O. M. Magnussen, Atomic-scale surface restructuring of copper electrodes under CO2 electroreduction conditions, *Nat. Catal. 2023 69*, 2023, **6**, 837–846.

28 J. de Ruiter, V. R. M. Benning, S. Yang, B. J. den Hartigh, H. Wang, P. T. Prins, J. M. Dorresteijn, J. C. L. Janssens, G. Manna, A. V. Petukhov, B. M. Weckhuysen, F. T. Rabouw and W. van der Stam, Multiscale X-ray scattering elucidates activation and deactivation of oxide-derived copper electrocatalysts for CO2 reduction, *Nat. Commun. 2025 161*, 2025, **16**, 1–11.

29 D. Cheng, K.-L. C. Nguyen, V. Sumaria, Z. Wei, Z. Zhang, W. Gee, Y. Li, C. G. Morales-Guio, M. Heyde, B. Roldan Cuenya, A. N. Alexandrova and P. Sautet, Structure Sensitivity and Catalyst Restructuring for CO2 Electro-reduction on Copper, *Nat. Commun.*, 2025, **16**, 4064.

30 Y. Hori, in *Modern Aspects of Electrochemistry*, 2008, pp. 89–189.

31 G. L. De Gregorio, T. Burdyny, A. Loiudice, P. Iyengar, W. A. Smith and R. Buonsanti, Facet-Dependent Selectivity of Cu Catalysts in Electrochemical CO2 Reduction at Commercially Viable Current Densities, *ACS Catal.*, 2020, **10**, 4854–4862.

32 K. Rossi and R. Buonsanti, Shaping Copper Nanocatalysts to Steer Selectivity in the Electrochemical CO2 Reduction Reaction, *Acc. Chem. Res.*, 2022, **55**, 629–637.

33 Y. Gao, Q. Wu, X. Liang, Z. Wang, Z. Zheng, P. Wang, Y. Liu, Y. Dai, M. H. Whangbo and B. Huang, Cu2O Nanoparticles with Both {100} and {111} Facets for Enhancing the Selectivity and Activity of CO2 Electroreduction to Ethylene, *Adv. Sci.*, 2020, **7**, 1–7.

34 R. M. Arán-Ais, R. Rizo, P. Grosse, G. Algara-Siller, K. Dembélé, M. Plodinec, T. Lunkenbein, S. W. Chee and B. Roldan Cuenya, Imaging electrochemically synthesized Cu2O cubes and their morphological evolution under conditions relevant to CO2 electroreduction, *Nat. Commun.*, 2020, **11**, 3489.

35 J. Vavra, T. Shen, D. Stoian, V. Tileli and R. Buonsanti, Real-time Monitoring Reveals Dissolution/Redeposition Mechanism in Copper Nanocatalysts during the Initial Stages of the CO_2 Reduction Reaction, *Angew. Chemie Int. Ed.*, 2021, **60**, 1347–1354.

36 P. Grosse, A. Yoon, C. Rettenmaier, A. Herzog, S. W. Chee and B. Roldan Cuenya, Dynamic Transformation of Cubic Copper Catalysts during CO2 Electroreduction and its Impact on Catalytic Selectivity, *Nat. Commun.*, 2021, **12**, 6736.

37 A. Yoon, J. Poon, P. Grosse, S. W. Chee and B. Roldan Cuenya, Iodide-mediated Cu catalyst restructuring during CO2 electroreduction, *J. Mater. Chem. A*, 2022, **10**, 14041–14050.

38 Y. Yang, S. Louisia, S. Yu, J. Jin, I. Roh, C. Chen, M. V. Fonseca Guzman, J. Feijóo, P. C. Chen, H. Wang, C. J. Pollock, X. Huang, Y. T. Shao, C. Wang, D. A. Muller, H. D. Abruña and P. Yang, Operando studies reveal active Cu nanograins for CO2 electroreduction, *Nature*, 2023, **614**, 262–269.

39 Y. Yang, C. Shi, J. Feijóo, J. Jin, C. Chen, Y. Han and P. Yang, Dynamic Evolution of Copper Nanowires during CO2 Reduction Probed by Operando Electrochemical 4D-STEM and X-ray Spectroscopy, *J. Am. Chem. Soc.*, 2024, **146**, 23398–23405.

40 Q. Zhang, Z. Song, X. Sun, Y. Liu, J. Wan, S. B. Betzler, Q. Zheng, J. Shangguan, K. C. Bustillo, P. Ercius, P. Narang, Y. Huang and H. Zheng, Atomic dynamics of electrified solid–liquid interfaces in liquid-cell TEM, *Nat. 2024 6308017*, 2024, **630**, 643–647.

41 R. Bro and A. K. Smilde, Principal component analysis, *Anal. Methods*, 2014, **6**, 2812–2831.

42 O. Christensen, A. Bagger and J. Rossmeisl, The Missing Link for Electrochemical CO2 Reduction: Classification of CO vs HCOOH Selectivity via PCA, Reaction Pathways, and Coverage Analysis, *ACS Catal.*, 2024, **14**, 2151–2161.

43 H. Y. Shi, Y. X. Chen, Y. H. Pu, H. L. Wang, Y. Z. Xie, X. Z. Tian, Y. Yang, A. S. She, W. Chen, W. H. Yang, X. M. Lin and C. Z. Lu, Regulation of electrode surface microenvironment by porous ion transport layer for High-Efficiency CO2 electrochemical reduction to ethylene, *Chem. Eng. J.*, DOI:10.1016/j.cej.2025.163490.

44 R. Reske, H. Mistry, F. Behafarid, B. Roldan Cuenya and P. Strasser, Particle size effects in the catalytic electroreduction of CO2 on Cu nanoparticles, *J. Am. Chem. Soc.*, 2014, **136**, 6978–6986.

45 H. Mistry, F. Behafarid, R. Reske, A. S. Varela, P. Strasser and B. Roldan Cuenya, Tuning Catalytic Selectivity at the Mesoscale via Interparticle Interactions, *ACS Catal.*, 2016, **6**, 1075–1080.

46 A. Wagner, C. D. Sahm and E. Reisner, Towards molecular understanding of local chemical environment effects in electro- and photocatalytic CO2 reduction, *Nat. Catal.*, 2020, **3**, 775–786.

47 P. P. Yang, X. L. Zhang, F. Y. Gao, Y. R. Zheng, Z. Z. Niu, X. Yu, R. Liu, Z. Z. Wu, S. Qin, L. P. Chi, Y. Duan, T. Ma, X. S. Zheng, J. F. Zhu, H. J. Wang, M. R. Gao and S. H. Yu, Protecting Copper Oxidation State via Intermediate Confinement for Selective CO2 Electroreduction to C2+ Fuels, *J. Am. Chem. Soc.*, 2020, **142**, 6400–6408.

View Article Online
DOI: 10.1039/D5EY00354G

Data Availability Statement

The data supporting the findings of this study can be found within the paper and the Supplementary Information file. Raw data files are available from the corresponding authors upon reasonable request